# A Dual-Polarization-Radar-Based Assessment of the 8 May 2003 Oklahoma City Area Tornadic Supercell

GLEN S. ROMINE

*University of Illinois at Urbana–Champaign, Urbana, Illinois*

DONALD W. BURGESS

*Cooperative Institute for Mesoscale Meteorological Studies, University of Oklahoma, and NOAA/National Severe Storms Laboratory, Norman, Oklahoma*

ROBERT B. WILHELMSON

*University of Illinois at Urbana–Champaign, and National Center for Supercomputing Applications, Urbana, Illinois*

(Manuscript received 31 July 2007, in final form 9 January 2008)

ABSTRACT

On 8 May 2003, a tornadic supercell tracked through portions of the Oklahoma City, Oklahoma, metropolitan area and produced violent damage along portions of its path. This storm passed through the dense in situ radar network in central Oklahoma and provided close-range operational, prototype polarimetric and terminal Doppler weather radar observations of the storm as it made the transition into the tornadic phase. The time-evolving polarimetric features were scrutinized with regard to storm morphology, particularly as related to the development of a rear-flank downdraft pulse within the storm immediately preceding the long-track tornado event. Two new polarimetric terms are introduced, the $Z_{dr}$ shield and $K_{dp}$ foot, along with a discussion of the orientation of the $Z_{dr}$ and $K_{dp}$ columns relative to midlevel rotation signatures. Storm downdraft and gust front characteristics are discussed relative to polarimetric fields and background environment characteristics. Highlighted for this event are a "warm" forward-flank downdraft and a particularly cold rear-flank downdraft. Emphasis is also placed on demonstrating key polarimetric field characteristics relative to traditional features at low and midlevels defined in familiar conceptual models of severe storms.

## 1. Introduction

A continuing challenge in the study of severe storms is assessing the tornadic potential of supercell storms with strong low-level mesocyclones. While an increasing body of evidence suggests that cold pools associated with significant tornado-producing supercell storms tend to have minimal departure from the inflow environment thermodynamic characteristics (e.g., Markowski et al. 2002; Shabbott and Markowski 2006; Grzych et al. 2007), the basis behind this finding is still not well understood. There has been speculation that colder rear-flank downdrafts (RFDs) may have a tendency to "undercut" the storm updraft, including the tornado cyclone region, and this negatively buoyant air opposes vertical ascent and the subsequent stretching that might otherwise lead to tornadogenesis (Brooks et al. 1994). Wakimoto and Cai (2000) noted even subtler differences between a pair of tornadic and nontornadic storms meticulously analyzed, with the tornadic storm exhibiting a warmer downdraft core as revealed from temperature retrieval methods. Unfortunately, the relationship between tornado potential and cold pool intensity is rarely of practical use in operational warnings since storm downdrafts are infrequently sampled by the sparse operational observing network relative to the size of storm cold pools. The thermodynamic characteristics of supercell downdrafts are thought to be regulated at least to some extent by a storm's microphysical

*Corresponding author address:* Glen Romine, Dept. of Atmospheric Sciences, University of Illinois at Urbana–Champaign, 105 S. Gregory St., Urbana, IL 61801.
E-mail: romine@atmos.uiuc.edu

DOI: 10.1175/2008MWR2330.1

makeup, as well as by the storm environment conditions and storm dynamics [see Markowski (2002) for a recent review of current understanding of rear-flank downdrafts]. Polarimetric radar observations provide information related to the time-evolving microphysical character of a storm (Straka et al. 2000). This information can potentially be utilized to help to elucidate the role that the microphysical character of hydrometeors may have in downdraft forcing, as well as subsequent surface thermodynamic characteristics of downdraft air relative to storm inflow. To help to reach the goal of better understanding polarimetric radar signatures, we detail the characteristics of a tornadic supercell, identifying prominent structures or evolution in select polarimetric fields that may provide insight into changes in storm character.

Polarimetric radars, which typically transmit energy and receive returned power at both horizontal and vertical orientations, offer supplemental observations related to differences in the orthogonal measurements in addition to the suite of products from conventional Doppler radars. Seliga and Bringi (1976) first introduced differential reflectivity (hereinafter $Z_{dr}$) and suggested that $Z_{dr}$ could be used to infer characteristics of a drop size distribution, with highly positive $Z_{dr}$ associated with large median volume diameter rain within the scattering volume. Later, Sachidananda and Zrnić (1987) developed a technique for deriving the specific differential phase (hereinafter $K_{dp}$). They noted that $K_{dp}$ could be used to improve rain-rate estimates. Notably, $K_{dp}$ was drawn from the differential phase, a field that Jameson (1985) showed was related to the liquid water content along the beam path. Thus, highly positive $K_{dp}$ measurements suggest radar volumes with substantial liquid water contents. Finally, correlation coefficient (hereinafter $\rho_{hv}$) was introduced by Balakrishnan and Zrnić (1990), which aided in discriminating mixed phase regions (such as radar volumes having both rain and hail) from radar volumes with homogeneous scattering particles.

A limited number of studies have sought to link signatures within these polarimetric fields to severe storm behavior and characteristics. Hall et al. (1984) provided early guidance in the field of hydrometeor classification, such as identifying rain by positive $Z_{dr}$ regions. They also first identified a narrow column of positive $Z_{dr}$ above the melting layer, which they presumed to be an indication of supercooled water. Later, Illingworth et al. (1987) linked $Z_{dr}$ columns to updrafts within developing convective cells. Thereafter, Conway and Zrnić (1993) and Brandes et al. (1995) supplemented polarimetric radar observations of $Z_{dr}$ columns with in situ aircraft observations of particle distributions and vertical velocity. In summary, these studies attributed the $Z_{dr}$ column signature to a deep vertical column of supercooled water extending well above the freezing level, offset slightly from the updraft maximum. They presumed that the collision and coalescence process within the updraft periphery allowed a sparse population of drops to grow to quite large sizes (up to 5 mm and therefore particularly oblate in shape).

Wakimoto and Bringi (1988) identified another feature they named a $Z_{dr}$ hole as a depression in the height of positive $Z_{dr}$ values below the melting level, which they associated with a wet microburst event. The microburst was presumably within a precipitation shaft where isotropic scattering from tumbling hailstones dominated the $Z_{dr}$ signature. The frequency of $Z_{dr}$ hole occurrences being associated with microburst events has not been widely studied. However, Scharfenberg (2002) examined several cases of microburst occurrences, and all were noted to have signatures consistent with the Wakimoto and Bringi (1988) model. Recent results from Ryzhkov et al. (2007) suggested that $Z_{dr}$ hole signatures may not be well detected by 5-cm-wavelength radars, which can have a resonance response that may obscure this signature.

Hubbert et al. (1998) further detailed a $K_{dp}$ column found adjacent to the aforementioned $Z_{dr}$ column and suggested this feature was caused by liquid drop shedding (preferentially in the 1–2-mm drop size range) from wet hailstone growth leading to high liquid water content regions aloft. Loney et al. (2002) then described in situ observations near the updraft at midlevels of a supercell thunderstorm and compared calculated polarimetric fields using aircraft-sampled particle distributions with polarimetric radar observations. Notably, they similarly related the $K_{dp}$ column to the melting and shedding of water drops along the left flank of the updraft. They also sampled a $Z_{dr}$ maximum along the right flank of the updraft at midlevels and sampled sparse larger drops within a region of the $Z_{dr}$ column. Schuur et al. (2001) described disdrometer measurements coupled with polarimetric radar observations for a supercell thunderstorm. They made note of a long-duration period where very large drops were sampled, but in very small concentration, beneath a continuous region of highly positive $Z_{dr}$ along the forward edge of a storm. Ryzhkov et al. (2005) later highlighted the presence of highly positive $Z_{dr}$ immediately downshear of the supercell storm updraft. They attributed this feature to size sorting owing to environmental vertical shear leading to large oblate drops in the radar volume. It should be noted that there are other possible interpretations for the large drop region. For example, Ulbrich and Atlas (2007) suggested that leading convec-

tive rains often have a narrow drop size spectrum with characteristics similar to an equilibrium drop size distribution (e.g., Hu and Srivastava 1995) with large median volume diameters. Finally, Ryzhkov et al. (2005) also illustrated polarimetric signatures of tornado debris that are largely composed of anisotropic scatterers yielding identifiable characteristics. Further applications of polarimetric radar signatures to flash flood forecasting and large hail detection were described in Scharfenberg et al. (2005).

Numerous studies have documented the structure and evolution of tornadic supercell thunderstorms (e.g., Browning 1964; Lemon and Doswell 1979; Doswell and Burgess 1993), largely rooted in analysis via conventional and Doppler radar observations. Yet, despite an increasing prevalence of polarimetric radar observations, to date no studies have documented the structure and morphology of polarimetric signatures associated with tornadic storms as they relate to traditionally accepted supercell models, aside from limited links to storm dynamic–thermodynamic characteristics described above. On 8 May 2003, a tornadic supercell passed through portions of the Oklahoma City (OKC), Oklahoma, metropolitan area causing up to F4 damage along its path. This violent storm tracked through portions of southwest Oklahoma City, the city of Moore, southeast Oklahoma City, Midwest City, and Choctaw, where the relatively dense in situ radar network in central Oklahoma afforded a unique dataset of multiplatform radar observations for subsequent analysis of this significant event.

This study builds on a preliminary investigation by Burgess (2004) of the 8 May 2003 storm event. Time variation of polarimetric field variables is demonstrated and spatial relations are shown between kinematic fields and polarization variables. Combined with aspects of the rear- and forward-flank downdraft evolution captured by multiplatform observations, the potential value of polarimetric radar trends as a possible window into storm cold pool traits is demonstrated. This work will hopefully inspire similar studies of other supercell events, both tornadic and nontornadic, to determine the generality of the findings described herein.

## 2. Data and methodology

The transition of the 8 May 2003 storm into its tornadic phase occurred in close proximity to the central Oklahoma fixed radar network, as the tornado tracked within 15 km of three Doppler radars and two aviation routine weather report (METAR) stations for the duration of the tornado event (see Fig. 1). The polarimetric observations for this case were collected by a proof-of-concept system at Norman, Oklahoma (KOUN), for the planned polarization upgrade of the fleet of operational Weather Surveillance Radar-1988 Doppler (WSR-88D; Doviak et al. 2000). KOUN collected continuous data [modified Volume Coverage Pattern-11 (VCP-11)[1]] from initiation through the transition into the tornadic phase of the storm. Thereafter, the radar suffered a power outage from tornado damage associated with the storm, limiting the time period of continuous collection to approximately 2048–2210 UTC on 8 May 2003. The precursor cells to the tornadic supercell developed within 70 km of the KOUN radar and passed within 30 km near the end of the observing period. While several convective features developed during the observing period within the detection range of the KOUN radar, the discussion here will focus on the cell that resulted in the significant tornado event in the Oklahoma City metro region—labeled cell B (hereinafter the OKC storm) in Fig. 2.

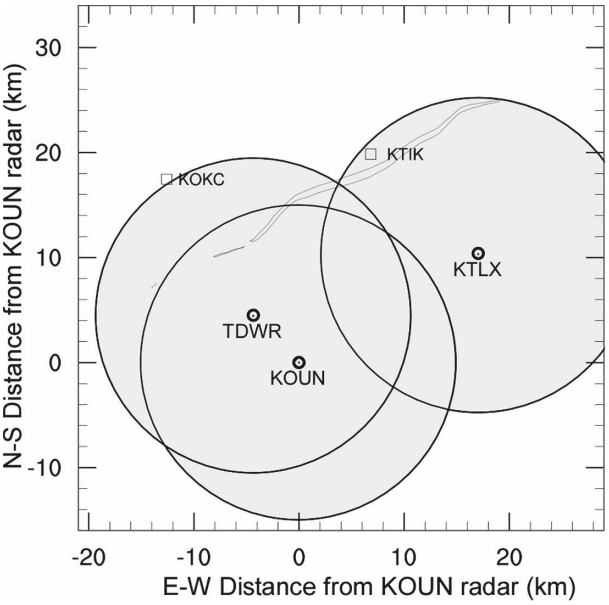


FIG. 1. Map of Doppler radars (KOUN, KTLX, and TDWR) and surface METAR locations (KOKC and KTIK) with the 8 May 2003 OKC tornado damage swath (thin black outline) plotted in reference to the location of the KOUN radar site. Rings of 15-km diameter are overlaid for each of the three radar locations to demonstrate the close-range coverage of the radar observations relative to the storm track.

Radar data collected from KOUN for this event were manually preprocessed to remove ground clutter and dealias radial velocities (Dowell et al. 2004). The

[1] See Schuur et al. (2003) for an overview of the KOUN scanning strategy.

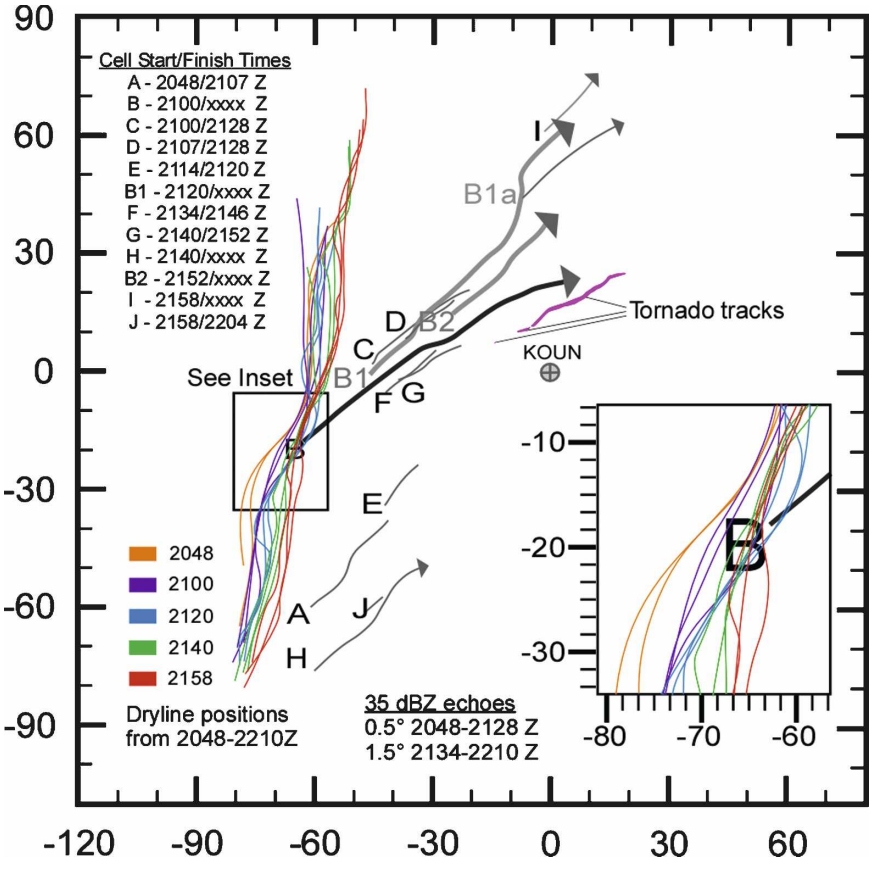


FIG. 2. Cell tracks and approximate dryline positions from 2046 to 2210 UTC 8 May 2003 for the "focus region," which was a 200-km$^2$ domain offset 10 km south and 20 km west of the KOUN radar site (which is at the origin) near Norman, OK. Cell centroids were tracked if two consecutive volume scans showed a distinguishable echo with ≥35 dB$Z$ using the 0.5° (1.5°) tilt scans from 2048 to 2128 (2134 to 2210) UTC. Dryline axis locations approximated from "clear air" returns on base scans, color coded by time window (time labels are first time in color grouping).

manual processing by Dowell et al. was extended to include the subjective removal of polarimetric fields from nonmeteorological returns (typified by very low $\rho_{hv}$ and highly "noisy" fields). Data volumes at central volume collection times were then created from the sweep sequences using echo translation with an assumed constant storm motion of 14 (8) m s$^{-1}$ in the E–W (N–S) direction. Data were then interpolated using a Cressman (1959) scheme with a 500-m radius from radar coordinates onto a Cartesian 1-km (500 m) horizontal (vertical) uniform grid. Notably, the time stamps on the KOUN radar products are believed to be ~150 s (±15 s) in error (fast) based on comparison with the WSR-88D in Twin Lakes, Oklahoma (KTLX), and the Terminal Doppler Weather Radar at Will Rogers World Airport, Oklahoma City (TDWR), products, and as such were adjusted prior to processing.

Additional radar observations from the KTLX WSR-88D (e.g., Crum and Alberty 1993) and TDWR (e.g., Vasiloff 2001) were also utilized for portions of this study, particularly for their time continuity (KTLX and TDWR), diverse view perspective (KTLX) relative to KOUN, and high temporal and spatial resolution of near-surface confluence boundaries (TDWR). The differences in the radar characteristics for systems used in this study are summarized in Table 1. Composites of the near-surface gust front evolution were created from spatially coherent radial convergence signatures in low-elevation scans from the KTLX and TDWR radars, translated using the mean storm motion to the volume collection times similar to the treatment of the KOUN observations. Differences in the timing between the base scans from KTLX and TDWR relative to the central volume collection times for the KOUN data volumes likely resulted in minor spatial inconsistencies between field overlays; however, they are still expected to

TABLE 1. Radar characteristics.

| Radar name | Location (°N, °W) | Elev (m) | Power (kW) | Pulse size (°, m) | Nyquist (m s$^{-1}$) |
|---|---|---|---|---|---|
| KOUN | 35.236, −97.462 | 381 | 750 | 0.95, 250 | Up to 2124 UTC<br>≤1.5° ± 12<br>≥2.5° ± 27.8<br>2126–2210 UTC<br>±27.8 |
| KTLX | 35.329, −97.282 | 385 | 750 | 0.95, 250* | ≤6.2° ± 26.1<br>7.5° ± 28.2<br>≥8.7° ± 30.4 |
| TDWR | 35.276, −97.510 | 384 | 250 | 0.55, 150 | ±22.4 |

* Range resolution of the reflectivity is reduced to 1000 m.

provide a meaningful qualitative overview of the gust front evolution relative to the polarimetric field morphology. Selected TDWR and KTLX scans used for the surface gust front evolution are summarized in Table 2. The relatively close range of the storm to the KTLX (TDWR) radar led to low-elevation beam height intersections with the gust front ranging from 300–600 (150–300) m above radar level around 2146 UTC to 120–300 (30–400) m above radar level by 2210 UTC.

Data collected from an operational sounding released by the National Weather Service Forecast Office (NWSFO) at Norman (adjacent to the KOUN radar site) around 0000 UTC 9 May 2003 is graphically summarized in Fig. 3. Also, a pair of METAR stations within the Oklahoma City metropolitan area sampled portions of the OKC storm's forward flank preceding tornadogenesis as well as during the mature phase of the tornado life cycle at close range (<1 km). The station locations relative to the regional radars are shown in Fig. 1. Meteograms of several meteorological variables are shown in Figs. 4 and 5 for the METAR stations at Oklahoma City (KOKC) and Tinker Air Force Base, Oklahoma (KTIK), respectively. Observations for both stations are available at irregular intervals during the shown period and as such connecting lines between observation points are provided only to demonstrate trends and may not accurately represent the actual rates of change.

TABLE 2. KTLX and TDWR scans utilized for gust front evolution.

| Radar name | Sweep start time (UTC) | Nearest volume time offset (s) | Beam elevation (°) |
|---|---|---|---|
| KTLX | 2146:16 | −16 to 2146 UTC | 0.5 |
| | 2151:14 | 46 to 2152 UTC | 0.5 |
| | 2156:10 | 110 to 2158 UTC | 0.5 |
| | 2206:04 | −124 to 2204 UTC | 0.5 |
| | 2211:01 | −61 to 2210 UTC | 0.5 |
| TDWR | 2146:24 | −24 to 2146 UTC | 0.5 |
| | 2152:24 | −24 to 2152 UTC | 0.5 |
| | 2158:23 | −23 to 2158 UTC | 0.5 |
| | 2205:31 | −91 to 2204 UTC | 1.0 |
| | 2211:31 | −91 to 2210 UTC | 1.0 |

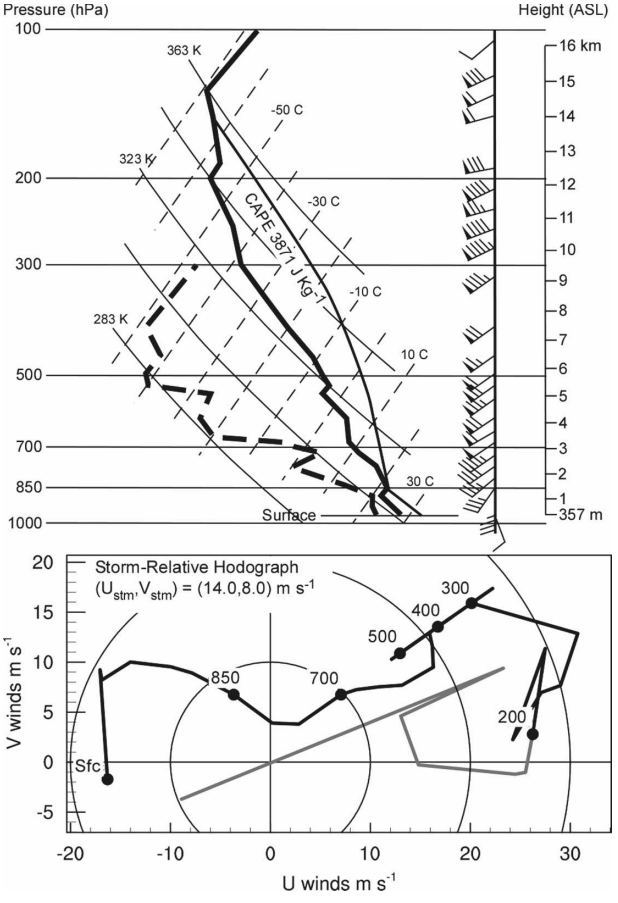


FIG. 3. Rawinsonde observations from the KOUN observing station for 0000 UTC 9 May 2003. (top) Temperature (heavy lines), dewpoint (heavy dashed lines), and 100-hPa mixed layer virtual parcel (thin lines) shown in skew $T$–log$p$ diagram format. Half, full, and pennant wind barbs are for 2.5, 5.0, and 50 m s$^{-1}$, respectively. (bottom) Storm-relative hodograph with winds (m s$^{-1}$) and mandatory pressure levels (hPa) indicated.

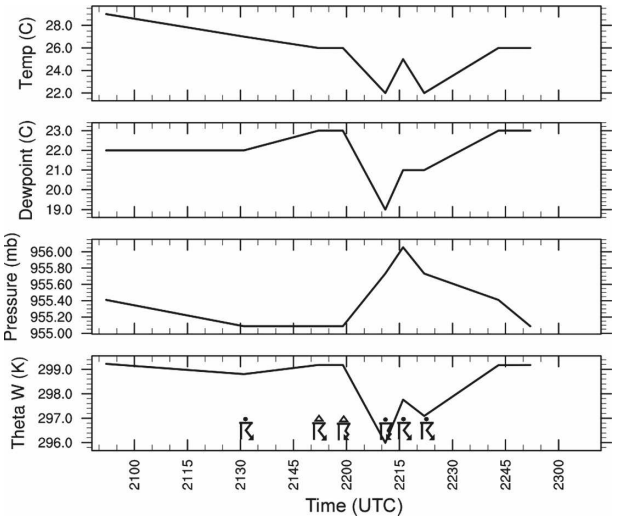


FIG. 4. Meteogram of observations from the KOKC METAR station for the period 2250–2300 UTC 8 May 2003. Variables shown are air temperature (°C), dewpoint temperature (°C), station pressure (hPa), wet-bulb potential temperature (K), and present weather (symbols). Severe hail (larger than 1.9 cm) was reported at the station at 2159 UTC.

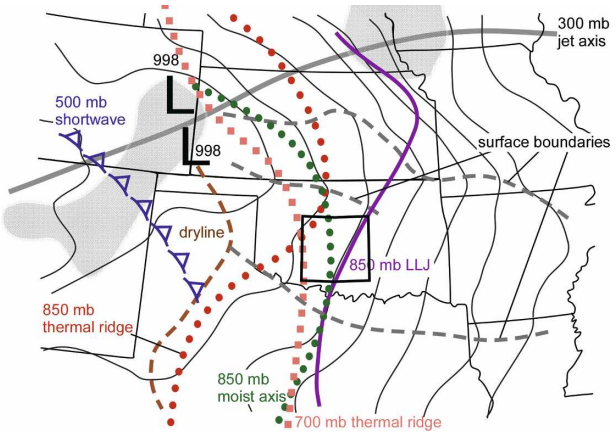


FIG. 6. Synoptic environment composite diagram for the southern plains at 1200 UTC 8 May 2003. Shown are 300-hPa jet axis (heavy gray line), 300-hPa divergence regions (stippled), 500-hPa short-wave axis (blue dashed line with triangles), 700-hPa thermal axis (peach squares), 850-hPa thermal and moist axes (red and green circles, respectively), 850-hPa low-level jet axis (purple heavy line), surface pressure contours every 2 hPa (thin gray lines), surface dryline (thin dashed brown line), and outflow boundaries (thin dashed gray lines). Local minima in pressure reduced to sea level are labeled with Ls.

## 3. Event overview

The synoptic weather pattern in place the morning of 8 May 2003 was typical of severe weather events in the southern plains (e.g., Doswell et al. 1993). This weather event was embedded within an extended severe weather outbreak summarized by Hamill et al. (2005). A zoomed-in composite chart (Miller 1972) for the southern plains region that morning (Fig. 6) showed a lee cyclone and attendant dryline poised to surge eastward as an upper-level short-wave trough approached the southern plains in west-southwesterly mean midlevel flow. A relatively deep layer of warm, moist air with origins from the Gulf of Mexico was already in place, contained by a strong capping inversion. With strong vertical wind shear profiles overlying the warm sector, the stage was set for a significant outbreak of severe storms by midafternoon. Synoptic-scale ascent associated with the approaching short wave as well as enhanced low-level convergence along the dryline and residual outflow boundaries from overnight convection combined with diurnal heating to allow scattered convective development across portions of Kansas by late afternoon, with more isolated storms farther south into central Oklahoma away from the stronger synoptic-scale ascent. For this study, attention is focused within a square region of 40 000 km$^2$ offset 10 km south and 20 km west of center over the KOUN radar site location (see Fig. 2).

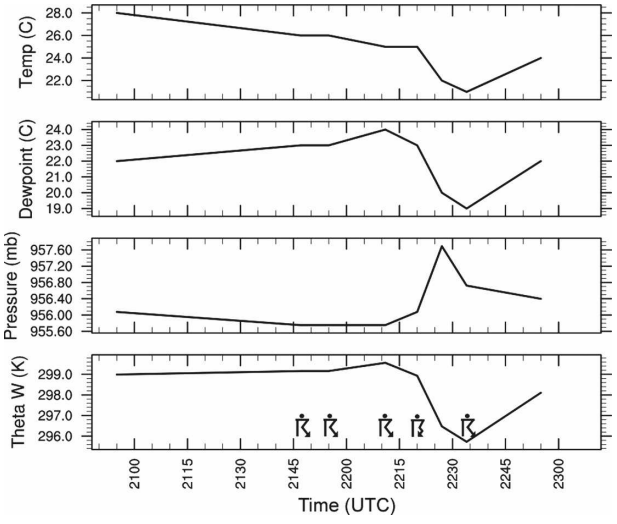


FIG. 5. As in Fig. 4, but for KTIK.

Lee et al. (2006) demonstrated that cell merger interactions may play an important role in subsequent storm behavior. As such, the early convective evolution for the 8 May storm was detailed owing to the possible impact this evolution had on later storm characteristics. Between 2000 and 2100 UTC a few clusters of small convective cells began developing just east of the dryline across western portions of central Oklahoma, which around 2026 UTC included a group near Apache, Oklahoma (~22 km SSW of Anadarko, Okla-

homa). The aforementioned storm cluster developed just south of a small-scale dryline bulge around 2030 UTC (see inset Fig. 2).

The 0000 UTC sounding from KOUN (Fig. 3, top) showed characteristics typical of Great Plains severe weather events. A relatively deep moist layer in the lower troposphere (mean water vapor mixing ratio of 16.9 g $kg^{-1}$ in the lowest 90 hPa) bounded by a modest capping inversion and steep midlevel lapse rates (850–500-hPa lapse rates $>7°C\ km^{-1}$) yielded 100-hPa mixed layer CAPE in excess of 3800 J $Kg^{-1}$. The environment freezing-level height was found near 4.2 km AGL while the freezing height for an ascending parcel was closer to 5.5 km AGL (for parcels in the updraft, the freezing height would more likely be somewhere between these heights owing to entrainment). The storm-relative hodograph (Fig. 3, bottom) showed significant veering of the low-level winds with height (0–3-km storm-relative environmental helicity $> 450\ m^2\ s^{-2}$) and substantial deep-layer shear (surface–6-km shear of 30 $m\ s^{-1}$) to support storm organization. As such, both a favorable kinematic and thermodynamic storm environment was in place for supercell and tornadic development. Given the modest large-scale forcing, it is hereinafter presumed that the KOUN sounding was representative of the background environment of the OKC storm.

All discrete cells that maintained a >35 dB*Z* echo for two consecutive volume scans (as sampled from KOUN) within the focus region were tracked during the main observing period (2048–2210 UTC) as illustrated in Fig. 2. The greatest concentration of cell tracks focused along a line from WSW to NNE of the radar including the tornadic cell (recall as track labeled B) near the axis of enhanced low-level moisture (Fig. 7). The OKC storm underwent two splits along its left flank during the observing period, generating tracks B1 and B2 at 2120 and 2152 UTC, respectively. Further, two immature cells merged with cell B along the right flank, cells F and G, at times 2140 and 2152 UTC, respectively.

The overall evolution of the OKC storm from 2100 to 2300 UTC can best be summarized using observations from the KTLX radar owing to its continuous data collection throughout the storm's lifetime. The early stages of the storm featured largely multicellular behavior with a gradual transition toward a more discrete classic supercell (not shown). A time–height diagram of the maximum reflectivity at each elevation angle (Fig. 8a) provides more detail about the storm's evolution. After a very short-lived first cell (~2040 UTC), a large, strong, tall cell developed by 2100 UTC and briefly produced 65 dB*Z* reflectivity aloft. The initial strong cell weakened and was replaced by a new rear cell (2121 UTC; first upward-pointing arrow in Fig. 8) that quickly strengthened. As indicated by the second and third upward-pointing arrows in Fig. 8, right-flank cells merged into the storm at 2141 and 2151 UTC. After the mergers, the storm grew very strong with a 70-dB*Z* core that extended to heights greater than 10 km above radar level (ARL). During the time period of the F4 tornado and the mesocyclone occlusion, the strong core descended toward the surface, presumably because of a weakening updraft. After 2230 UTC, no elevated, highly reflective core was detected, although a large area of 60-dB*Z* reflectivity continued.

A companion time–height diagram of the maximum azimuthal shear or azimuthal vorticity (the component of vertical vorticity sensed by a single-Doppler radar) at each elevation angle (Fig. 8b) provides more details about the mesocyclone evolution. Azimuthal vorticity data are derived from an algorithm that uses two-dimensional linear least squares estimates of radial velocity derivatives (LLSDs; Smith et al. 2003). The input data are averaged and have a calculation kernel of mesocyclone size (5 km) passed over them. The mesocyclone strength vorticity did not exist at any height within the storm during the storm's early life (prior to 2121 UTC). After the development of the new rear cell (2121–2141 UTC), weak mesocyclone-strength vorticity values began to occur aloft. During and after the merger of the two flanking cells (2141 UTC and beyond), values aloft rapidly increased to the strong mesocyclone category, reaching a maximum of about $30 \times 10^{-3}\ s^{-1}$ at 4–5-km height at tornado time. Radial convergence below cloud base increased markedly preceding the development of significant low-level vorticity and subsequent tornadogenesis, in line with previous studies (Burgess and Magsig 1993, 1998). Notably, careful analysis of close-range, high temporal resolution TDWR base data strongly suggested a single tornado event originating near 2206 UTC, which differs in tornadogenesis time (2 min later) and the segmented path detailed in official NWS survey results and the National Climatic Data Center *Storm Data* publication (NCDC 2003, 340–342) listed as the second and third tornadoes. The first reported brief tornado near 2200 UTC was not evident in products from any of the radars. Nevertheless, the elevated mesocyclone vorticity maxima gradually weakened and descended toward the surface during the tornado's lifetime. The completion of the occlusion process brought an end to the life of the tornado-parent mesocyclone center at about 2250 UTC. A pair of subsequent circulation centers sequentially developed with the storm, maintaining the supercell well beyond 2300 UTC, yet neither was as strong as the prior

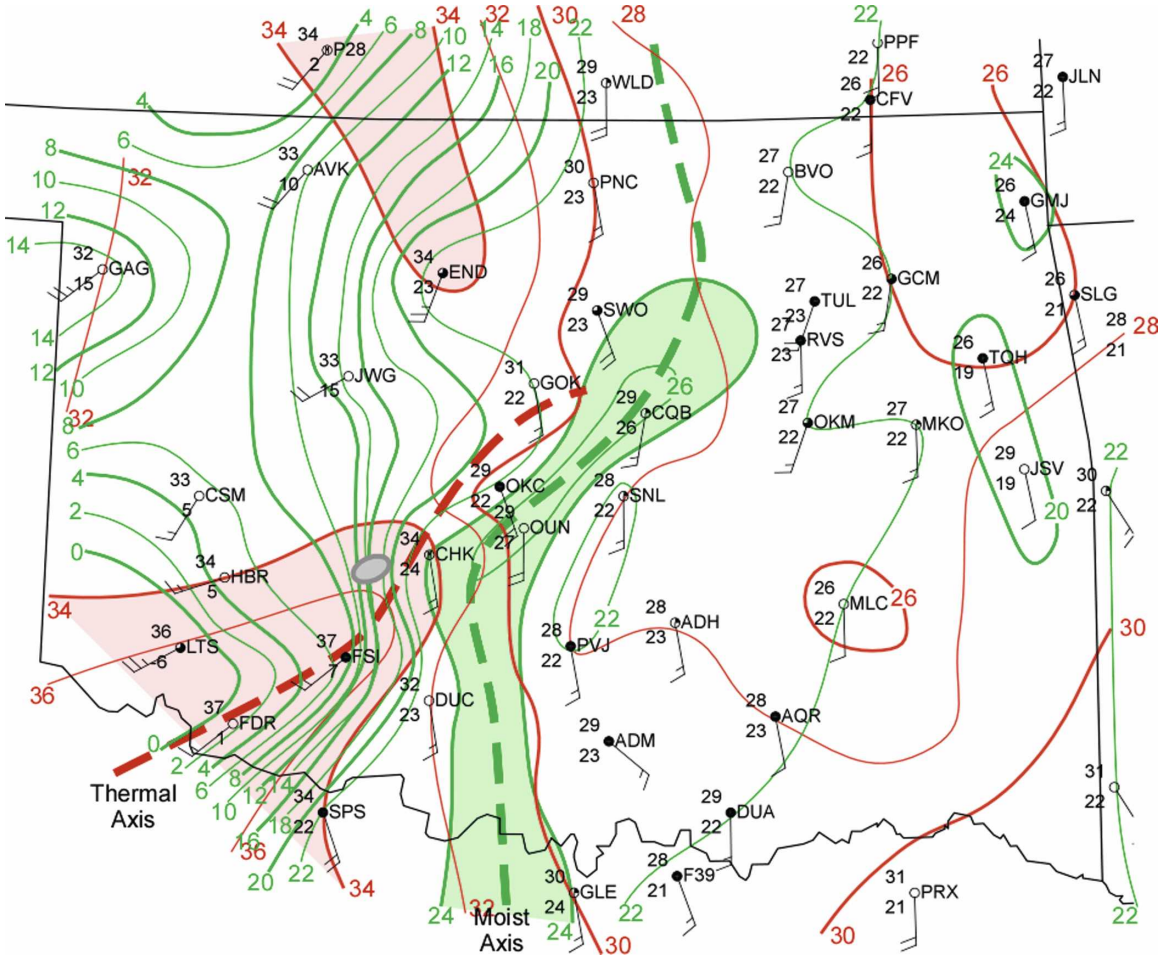


FIG. 7. Surface station observations at 2100 UTC 8 May 2003. Each station is labeled with air temperature (°C; top left), dewpoint (°C; bottom left), station identifier (right), cloud cover (center fill, where open represents clear), and wind speed and direction (half barb, 5 kt; full barb, 10 kt). Overlaid are subjectively derived contours of air temperature (red; regions greater than 34°C are filled) and dewpoint every 4°C (green; areas greater than 24°C are filled), along with the approximate region of storm initiation (gray filled area WSW of Chickasha, OK).

tornadic circulation, and no more tornadoes were reported with this storm.

## 4. Discussion of polarimetric field observations

### *a. Early polarimetric field evolution (2100–2140 UTC)*

The OKC storm evolved from a disorganized multicell cluster into a discrete supercell with strong midlevel rotation during this period. Within the polarimetric fields, early cell evolution demonstrated several of the characteristic polarimetric field structures previously described in the literature, such as $Z_{dr}$ and $K_{dp}$ columns. In particular, the OKC storm possessed intermittent positive $Z_{dr}$ columns (here defined as a vertically contiguous region of $Z_{dr}$ of 3 dB or greater extending above the freezing level) during its formative stages. These columns typically appeared along the upshear echo edge of cells both embedded within the early multicell structure and other distinct cells. Intermittent $K_{dp}$ columns (here defined as a vertically contiguous region of 1.5° km$^{-1}$ or greater) also appeared downshear of persistent $Z_{dr}$ columns during the early stages of convective organization and were a well-established feature with the OKC storm beyond 2120 UTC coincident with new rear-cell development and associated weak midlevel updraft rotation (Fig. 8b). The first left split (cell B1) was traced back to a small $Z_{dr}$ column that developed along the forward left flank of the precursor OKC storm around 2108 UTC. As a new rear cell merged into the OKC storm from 2120 to 2134 UTC, an attendant $Z_{dr}$ column developed and merged aloft with

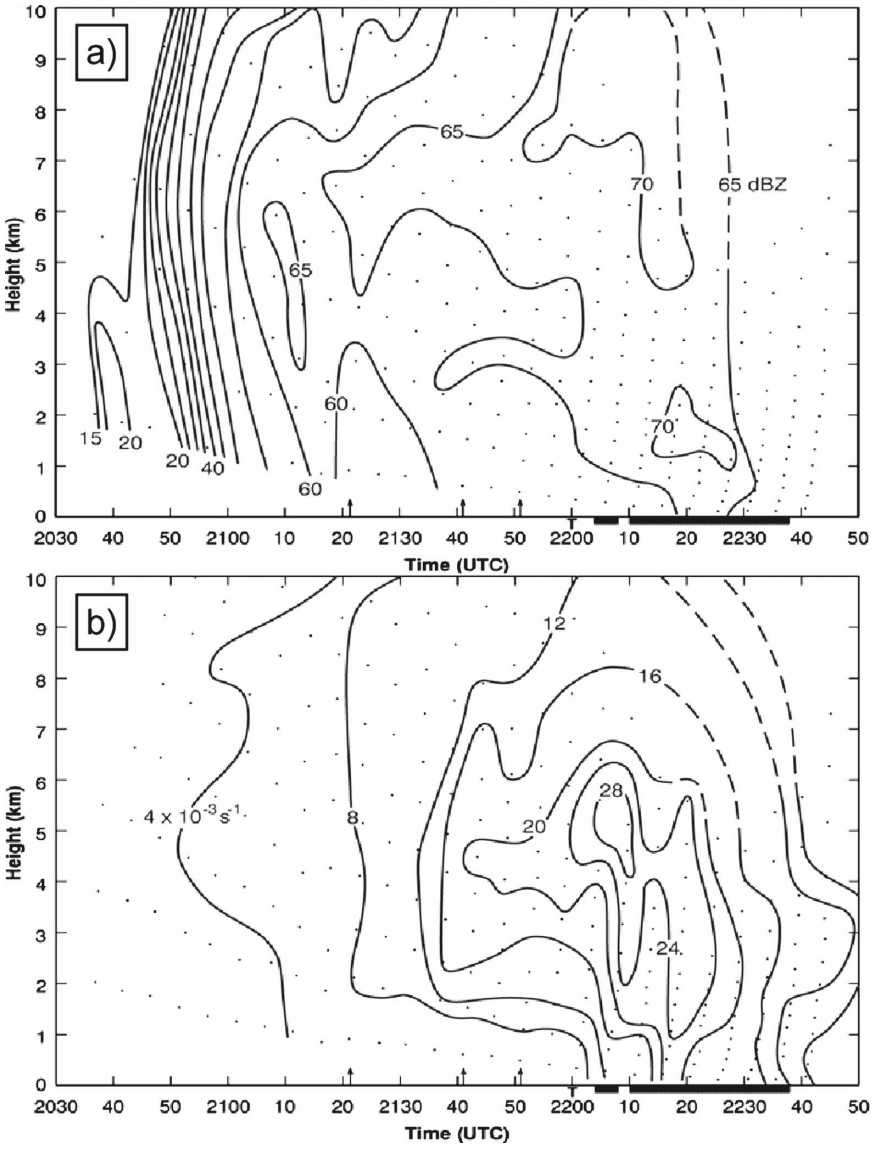


FIG. 8. Time–height diagrams of (a) reflectivity and (b) azimuthal vorticity from the KTLX radar. Dots are individual data points. Upward-pointing arrows along the *x* axis mark cell changes. Dark bars and the T along the *x* axis indicate tornado times.

the preexisting $Z_{dr}$ column. Simultaneously, the $K_{dp}$ column shifted counterclockwise relative to the $Z_{dr}$ column. A region of high $Z_{dr}$ well below the melting level developed downshear of the updraft, with higher peak values particularly along the right flank of the dominant cell (this feature is hereinafter referred to as the $Z_{dr}$ shield). Thus, the development of a $Z_{dr}$–$K_{dp}$ column couplet along the upshear edge of the storm echo coincided with the appearance of a strong midlevel mesocyclone (Fig. 8b), as well as the development of the $Z_{dr}$ shield downshear of the updraft. Notably, the orientation of the $Z_{dr}$ column lying along the left flank of the updraft differs from the observations described in Brandes et al. (1995) of a multicell hailstorm where the $Z_{dr}$ column was instead downshear of the main updraft.

### *b. Mature supercell polarimetric field characteristics and evolution (2146–2204 UTC)*

The OKC storm, which as noted earlier acquired strong midlevel rotation by 2140 UTC, later absorbed a second right-flank merger while simultaneously displacing a second left split (cell B2) near the 2152 UTC time frame. Thereafter, a rear-flank downdraft pulse swept cyclonically across the back edge of the storm from the left- to the right-rear flank by 2158 UTC. Subsequent

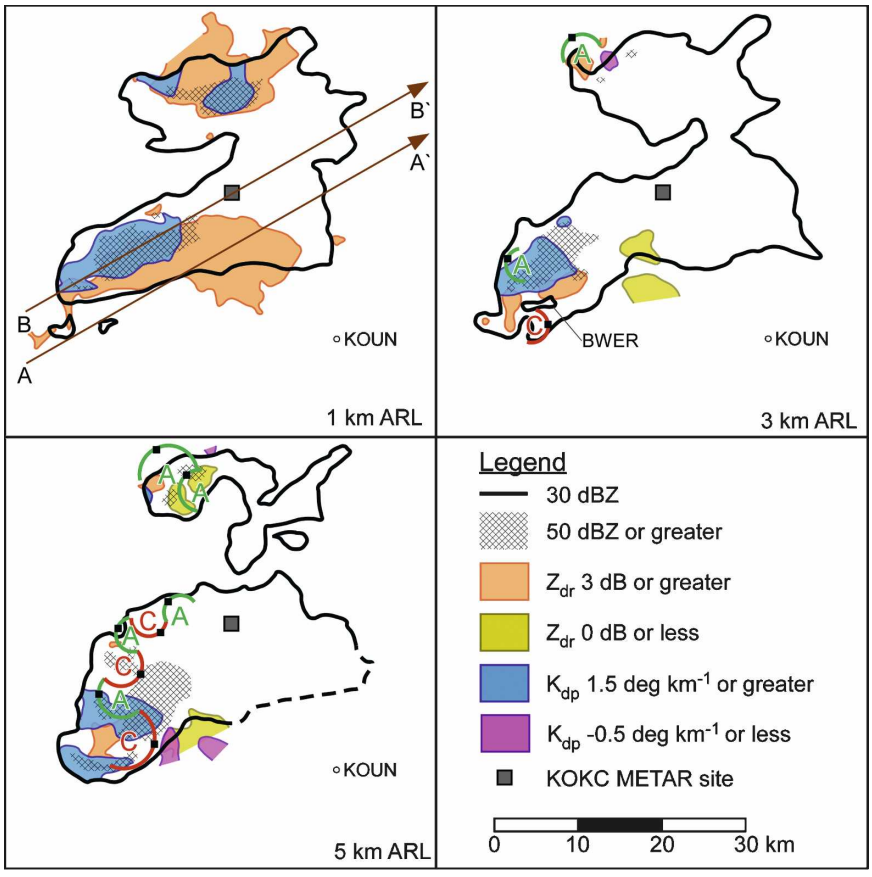


FIG. 9. CAPPI plots at (top left) 1, (top right) 3, and (bottom left) 5 km ARL at 2146 UTC with 30-dB$Z$ contour of the radar reflectivity (heavy black) (dashed contours are extrapolated estimates within the radar's cone of silence) and regions with 50 dB$Z$ or greater hatched; (bottom right) regions of $Z_{dr} \geq 3$ and $\leq 0$ dB and $K_{dp}$ areas $\geq 1.5$ and $\leq -0.5°$ km$^{-1}$ color filled following the legend. Additionally, cyclonic (anticyclonic) azimuthal shear is shown by red (green) half-circles between opposing storm-relative radial wind maxima with shear centroids labeled as C (A), and black boxes indicating couplet alignment relative to the radar position (radial convergence–divergence).

strong low-level convergence along the lead edge of the rear-flank gust front preceded the development of a strong low-level mesocyclone and tornadogenesis near 2204 UTC. This event sequence is now considered with regard to both the quasi-steady and evolving aspects of the polarimetric fields during this critical period. Figures 9–13 provide key polarimetric field overlays shown on constant altitude plan position indicator (CAPPI) surfaces at 1, 3, and 5 km ARL from 2146 through 2210 UTC. Vertical cross sections aligned along the storm motion vector, oriented as shown in the upper-left panels of Figs. 9–13, provide additional insight into the vertical structure of select polarimetric features (Figs. 14–17). Discussion will begin with notable quasi-steady elements followed by the time-evolving features.

A persistent element at 1 km ARL included a large area of significant positive $Z_{dr}$ ($\geq$+3 dB) along the right-forward flank of the storm, the "$Z_{dr}$ shield," which generally was broadest far downshear of the updraft and more tapered along the upshear extent. Recall that the highly positive $Z_{dr}$ values are consistent with scattering from large oblate raindrops (e.g., Bringi and Chandrasekar 2001). When highly positive $Z_{dr}$ values are collocated with modest reflectivity values and small $K_{dp}$, relatively sparse drop populations would be expected (Straka et al. 2000) and subsequently would provide an inefficient source of evaporative cooling at low levels within the $Z_{dr}$ shield (Pruppacher and Klett 1997). Thus, the presence of a wide $Z_{dr}$ shield along the right-forward flank of a tornadic supercell would be consistent with observations of weak baroclinicity along the right-forward flank (Shabbott and Markowski 2006). The depth of the $Z_{dr}$ shield as here defined was persistently rather shallow (Figs. 14–17), generally be-

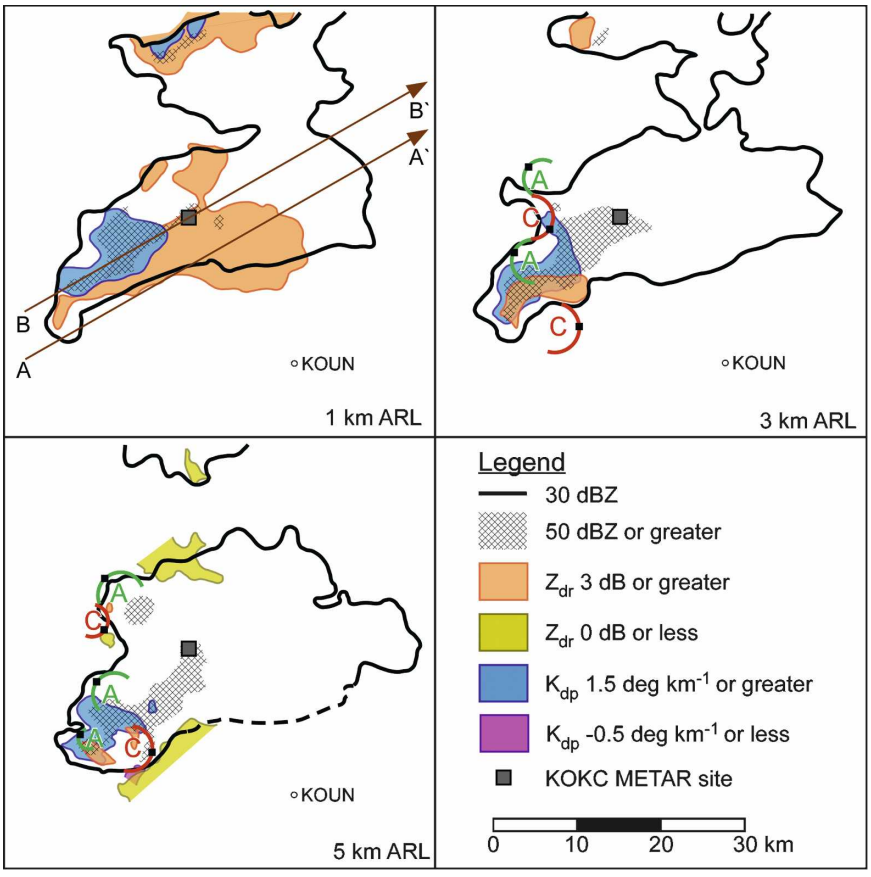


FIG. 10. As in Fig. 9 but valid at 2152 UTC.

low 2 km, whereas the height of the melting level from the environment was closer to 4.2 km ARL (see Fig. 3). Physical processes that might explain this difference included the lower height of the wet-bulb melting level relative to the melting height. Further, even once ice particles begin melting, continued falling of the hydrometeors would have occurred until there was sufficient melting to change the dominant scattering media characteristics from those typical of larger ice species such as frozen drops, hail, or graupel (with $Z_{dr}$ values closer to zero) to that of rain. Finally, self-collection of melted water drops would have become increasingly likely as the water content increased from melting particles in the column, which would have shifted the median volume drop diameter upward, with increased $Z_{dr}$ values, with peak values controlled by balanced drop breakup. A summary of other plausible mechanisms for the development of narrow large drop spectra is included within Rosenfeld and Ulbrich (2003).

Aligned nearer the echo centerline of the storm at 1 km ARL was a downshear elongated $K_{dp}$ maximum, hereafter referred to as the $K_{dp}$ foot, from well left of the storm updraft and adjacent to and overlapping the left edge of the $Z_{dr}$ shield. Note from the meteogram observations at the KOKC METAR site (Fig. 4) that large hail reports coincided with the passage of the lead edge of the $K_{dp}$ foot overtaking the site (Figs. 14 and 15, top). From further examination of Figs. 14–17 it is apparent that the downshear extension of the $K_{dp}$ foot lies beneath and eventually within a descending high-reflectivity center as it extended below the melting level. This reflectivity core appears to originate near the top and downshear of the $K_{dp}$ column aloft. Near the centroid of the $K_{dp}$ foot, the $Z_{dr}$ values are locally lower along with a minimum in $\rho_{hv}$ below the melting level (not shown), presumably owing to the presence of a hail shaft (e.g., Bringi et al. 1986; Brandes et al. 1995; Hubbert et al. 1998), and may also identify a downdraft source region (e.g., Wakimoto and Bringi 1988; Knupp 1988) within the forward flank of the storm. The $K_{dp}$ foot is contiguous with the $K_{dp}$ column aloft along the upshear edge. From 2134 to 2204 UTC, both the $Z_{dr}$ shield and especially the $K_{dp}$ foot expanded considerably in spatial extent at 1 km ARL (approximately 2 and 5 times larger, respectively).

Shifting attention aloft, as noted earlier the $Z_{dr}$ and

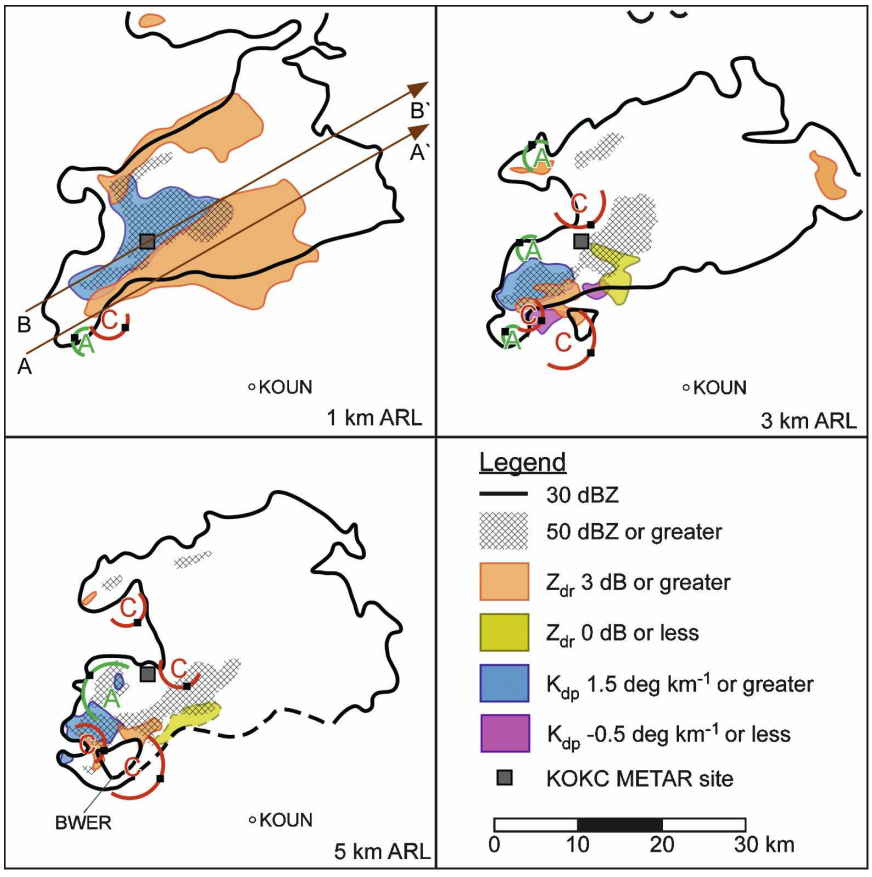


FIG. 11. As in Fig. 9 but valid at 2158 UTC.

$K_{dp}$ columns extend above the upshear edge of the $Z_{dr}$ shield and $K_{dp}$ foot, respectively. The $Z_{dr}$ column encompassed the storm updraft prior to 2140 UTC but by 2146 UTC was collocated with the bounded weak echo region of the storm. From 2158 UTC and beyond, the higher $Z_{dr}$ values eroded along the right flank of the updraft yet persisted along the left edge of the storm updraft, adjacent to the $K_{dp}$ column. The location of the $Z_{dr}$ column to the left-rear flank relative to the storm updraft location was similar to the borderline supercell case described in Conway and Zrnić (1993). Transient negative $Z_{dr}$ regions were also noted above the $Z_{dr}$ column and particularly near the top of the $K_{dp}$ column in the range of 6–8 km AGL, generally accompanied by low $\rho_{hv}$. From 2146 to 2210 UTC, the midlevel mesocyclone motion deviated sharply rightward relative to the tracks of the $Z_{dr}$ and $K_{dp}$ columns, particularly between 2158 and 2204 UTC as anticyclonic shear strengthened along the upshear side of the mesocyclone. There were also expanding regions of negative $Z_{dr}$ and $K_{dp}$ aloft downshear of the storm updraft at midlevels, suggesting the presence of prolate and/or vertically oriented particles in this portion of the storm overlaying the right flank of the $Z_{dr}$ shield (Bringi and Chandrasekar 2001). The $Z_{dr}$ and $K_{dp}$ columns were flanked by midlevel counterrotating azimuthal shear centers. This yielded a perturbation flow pattern that enhanced the rearward transport of supercooled liquid water toward a region of midlevel radial convergence (not shown) along the upshear edge of the $K_{dp}$ column. This flow may have also contributed to the apparent upshear tilt of the $K_{dp}$ column with height toward the end of the period.

Figure 18 provides a summary view of the low-level polarimetric field evolution relative to the near-surface gust front positions presented in a ground-relative framework from 2146 through 2210 UTC. Recall that near 2152 UTC a new cell merged with the main echo along the right-rear flank while an anticyclonic cell split off the storm's left flank. From base-scan radial velocity convergence signatures collected by KTLX and TDWR, near-surface boundaries were mapped during the focus period and overlaid with the nearest in time KOUN volume collection windows. The boundary that extended farthest downshear (upshear) and oriented quasi-parallel (quasi perpendicular) to the storm motion vector will hereinafter be referred to as the for-

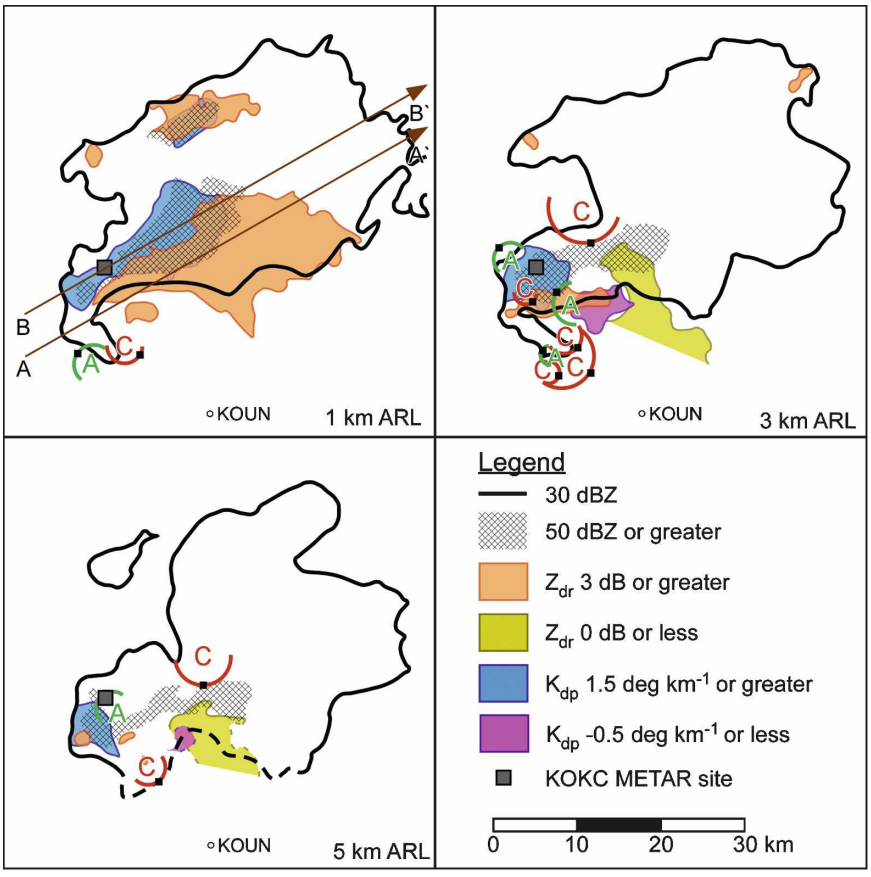


FIG. 12. As in Fig. 9 but valid at 2204 UTC.

ward-flank (rear flank) downdraft gust front. Owing to the boundary orientations relative to the two radars, the rear- (forward-) flank gust front was predominantly mapped from the KTLX (TDWR) radar perspective.

The main rear-flank downdraft surge originated along the left-rear quadrant of the storm (near −32, 8 km) at 2146 UTC northwest of a lead forward-flank gust front (FFGF). The leading edge of rear-flank downdraft surge then swept rapidly southeastward overtaking the FFGF by 2158 UTC, then bulging east

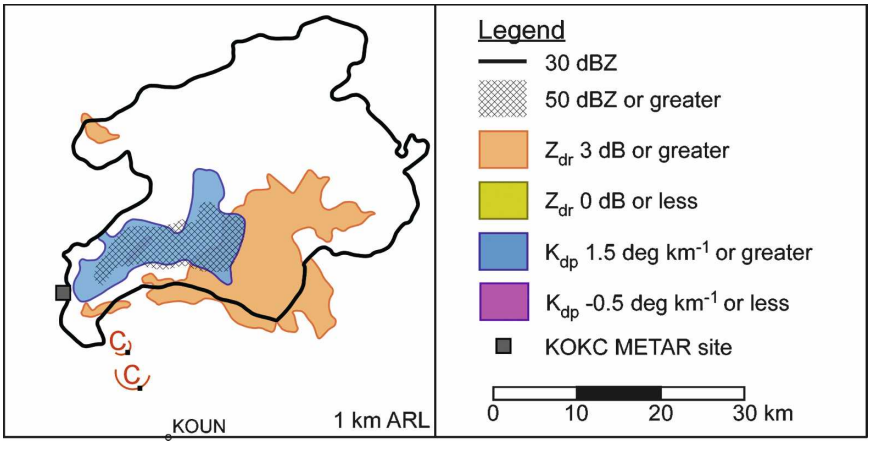


FIG. 13. As in Fig. 9 but valid at 2210 UTC, and only for the 1-km CAPPI plot.

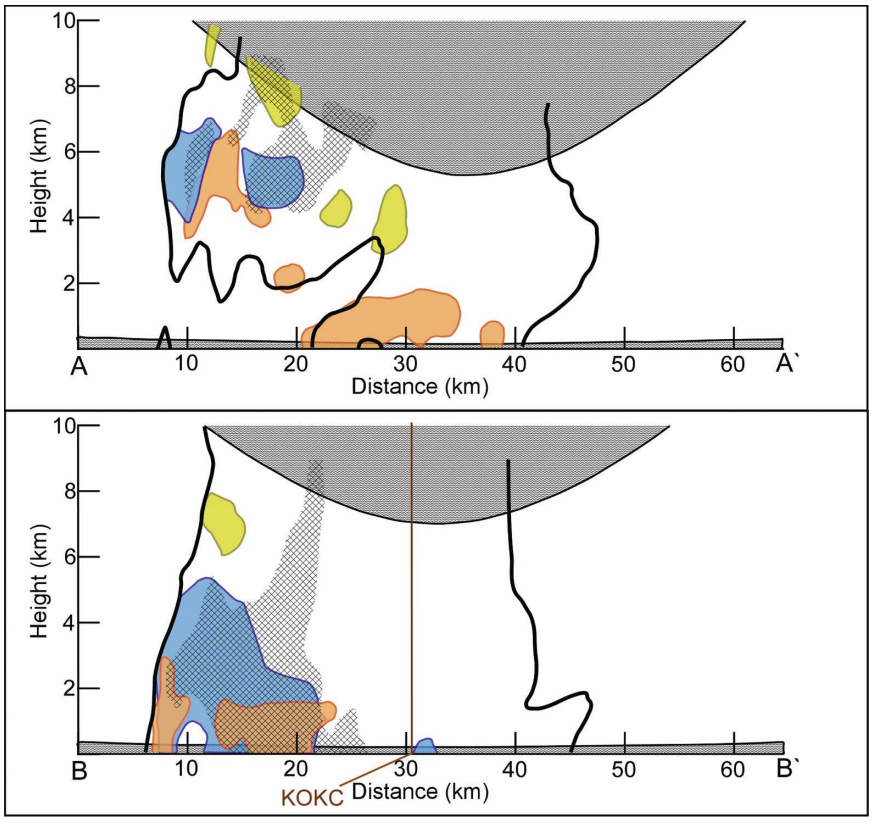


FIG. 14. Vertical cross sections aligned (top) along the storm motion vector slicing through the storm updraft region (A–A′) and (bottom) to pass over the KOKC METAR station (B–B′) with the position of KOKC indicated in the bottom panel as a vertical brown line valid at 2146 UTC volume time. Areas above the radar's cone of silence and below the radar horizon are gray filled in the background. Overlays are otherwise the same as in Fig. 9, with the orientation of the cross sections as shown over the 1-km CAPPI plot.

and eventually east-northeast in a cyclonic arc at a fairly uniform speed near 20 m $s^{-1}$. The rear-flank gust front (RFGF) expanded along the entire back edge of the storm, roughly perpendicular to the storm motion, though with the surge only along the right flank. Surface observations indicated that the RFGF overcame the KOKC station near 2159 UTC. The upshear edge of the $K_{dp}$ foot also passed over KOKC about this time. The evolution patterns of the FFGF(s) were more variable than the RFGF, but generally featured one weakly convergent boundary along the right flank of the echo edge and another closer to the echo centerline, but right of the clockwise-shifting $K_{dp}$ maximum. These boundaries merged with the RFGF, not where the tornado cyclone developed but offset several kilometers toward the left flank. Note also that during this time window the $K_{dp}$ maximum shifted from adjacent to the left-rear edge of the $Z_{dr}$ maximum to the left-forward edge. The$K_{dp}$ foot region consistently featured divergent radial velocity signatures at low levels. Since the $K_{dp}$ foot was beneath a $Z_{dr}$ hole signature, which has been suggested as a source for downdraft forcing (Wakimoto and Bringi 1988), it is suggested the $K_{dp}$ foot may serve as a rough indicator for the location of the forward-flank downdraft core.

### c. *Forward- and rear-flank downdraft sources*

The sounding shown in Fig. 3 is now examined in greater detail, particularly with regard to low-level thermodynamics in pursuit of candidate levels for the origin of the observed rear-flank downdraft. The sounding reveals a surface-based layer that was topped by a shallow, stable capping inversion with a conditionally unstable layer and another relatively well mixed dry-adiabatic layer farther aloft. Table 3 lists select thermodynamic variables derived from the KOUN sounding as well as the forward (F-XXX) and rear (R-XXX) flank downdraft samples from the KOKC and KTIK observing stations, sorted by descending wet-

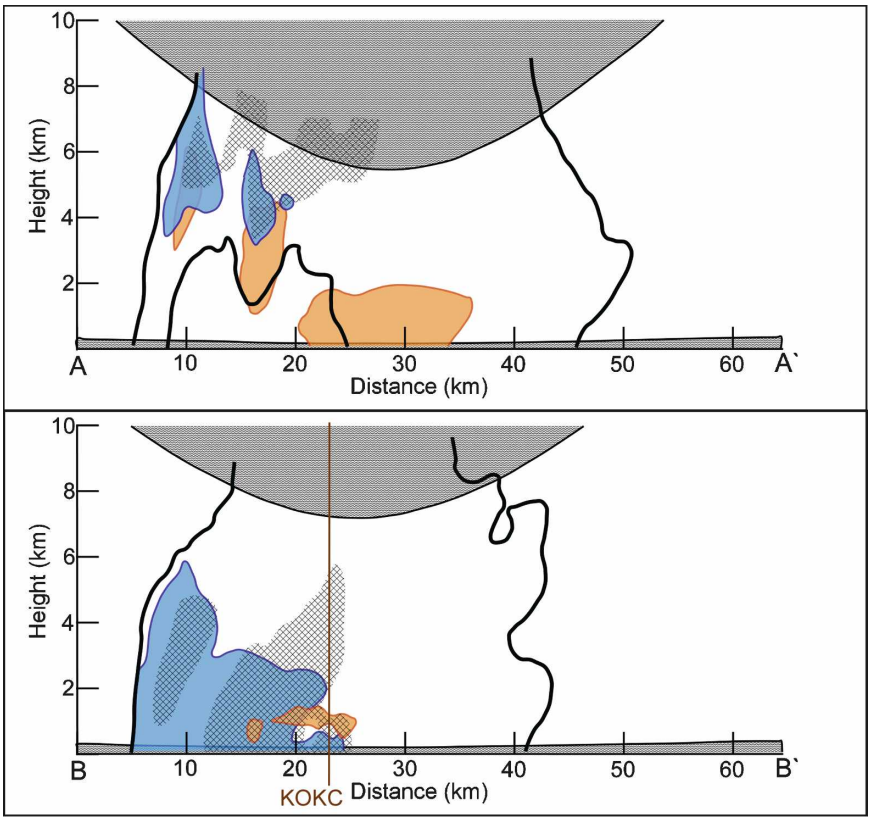


FIG. 15. As in Fig. 14 but valid at 2152 UTC.

bulb potential temperature. The forward-flank characteristics were similar to the surface layer environment, whereas the rear-flank samples were more similar to the conditionally unstable layer above the inversion. It was previously suggested that the forward-flank downdraft core appeared to have its source within the low-level $K_{dp}$ maximum region, the centerline of which tracks very near the KOKC site. Sampling of storm outflow properties was limited to points entirely north of the tornado track at different stages in the storm behavior. Nevertheless, both sampled very similar thermodynamic conditions both ahead and behind the RFGF. The forward-flank downdraft thermodynamic characteristics suggested entrainment of very little, if any, environmental air within this downdraft from above the surface inversion as both stations reported surface temperatures and dewpoints that approached wet-bulb temperatures characteristic of the surface layer. Srivastava (1987) and Knupp (1988) both suggested that melting processes can be a significant downdraft source for negative buoyancy in shallow downdrafts. As previously noted, the downshear edge of the $K_{dp}$ foot signature was consistent with hail particles descending below the melting layer, as well as observations of severe hail reported within the $K_{dp}$ foot signature area. As such, it appears possible that in this case melting hail may have contributed negative buoyancy, enhancing the forward-flank downdraft, though perhaps not enough so aloft for the downdraft to have origins above the inversion layer. The high liquid water content within the $K_{dp}$ foot would also contribute to precipitation drag effects aiding in the dynamic forcing for the forward-flank downdraft.

By contrast, the rear-flank downdraft air appears too cool and dry to not have at least some source air originating from 1.4 km MSL or above, depending on the degree of entrainment. By example, within the vicinity of 2–3 km MSL, modest moistening of environmental air would have led to significant negative buoyancy favorably poised to accelerate toward the surface, potentially penetrating the capping inversion. Favorable radial convergence parallel to a strong gradient in $K_{dp}$ (liquid water content) persisted on the left-rear flank of the storm during the window of rear-flank downdraft surge development previously detailed in section 4b. A later foci of strong radial convergence also developed on the right-rear flank (begins 2152 UTC, strong by 2158 UTC) as the cyclonic anticyclonic shear pair raced

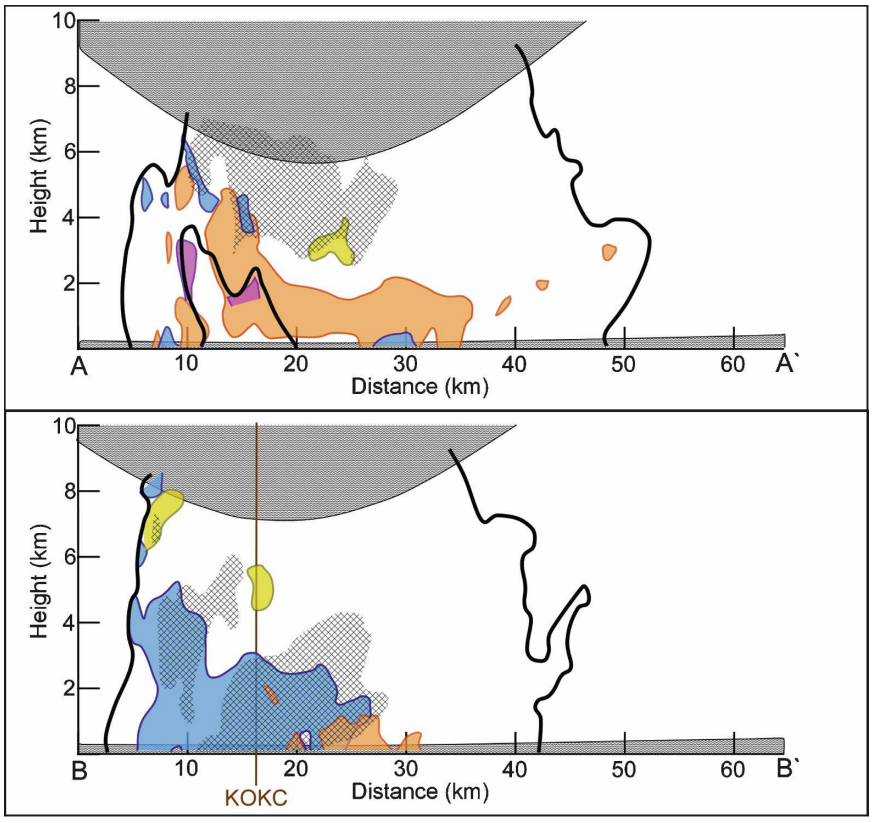


FIG. 16. As in Fig. 14 but valid at 2158 UTC.

toward the mesocyclone core with a thin strand of precipitation in its wake. However, there appears to be only modest liquid water content associated with this secondary convergence maximum and as such a reduced confidence that this also served as a source region for the thermodynamic downdraft forcing. The cool and dry conditions within the RFD of this storm stand out from the general finding of Markowski et al. (2002) of minimal departure in equivalent potential temperature relative to the environmental conditions for significant tornadic supercells. The exception case they noted (case 21) also resulted in a violent, long-duration tornado, with upper-range deficits similar to those observed for the OKC storm, on the order of 15–20 K.

A noteworthy aspect from our analysis of this case was the rather warm surface conditions within the forward-flank portion of the storm, suggestive of a shallow forward-flank downdraft below the environment inversion layer. The forward-flank downdraft core was likely aided by cooling from the melting of large hail (e.g., Srivastava 1987; Knupp 1988), though perhaps relatively modest concentrations of small drops were present despite significant liquid water content within the shallow layer. By contrast, the rear-flank downdraft source region featured a deep column of high liquid water content, and may have also benefited from updraft and environment vertical shear interaction contributing to downdraft forcing in this region of the storm (e.g., Rotunno and Klemp 1982).

### *d. Fit of polarimetric observations to a conceptual supercell model*

Conceptual models of severe storms have often been employed as an aid in gaining greater insight into a storm's behavior, characteristics, and the interrelations between storm features. While conceptual models rarely fit exactly with any particular event, models have nevertheless often been constructed based on prototypical case studies, such as the classic supercell models proposed by Lemon and Doswell (1979, their Fig. 7) and Doswell and Burgess (1993, their Fig. 3a). The Lemon and Doswell model features a highly occluded tornado cyclone, whereas the Doswell and Burgess model represents a more "open wave" type surface gust front analogy (without tornado). The latter is a better fit to the OKC storm prototype and is similar to the inflow and outflow balanced 8 June 1995 McLean,

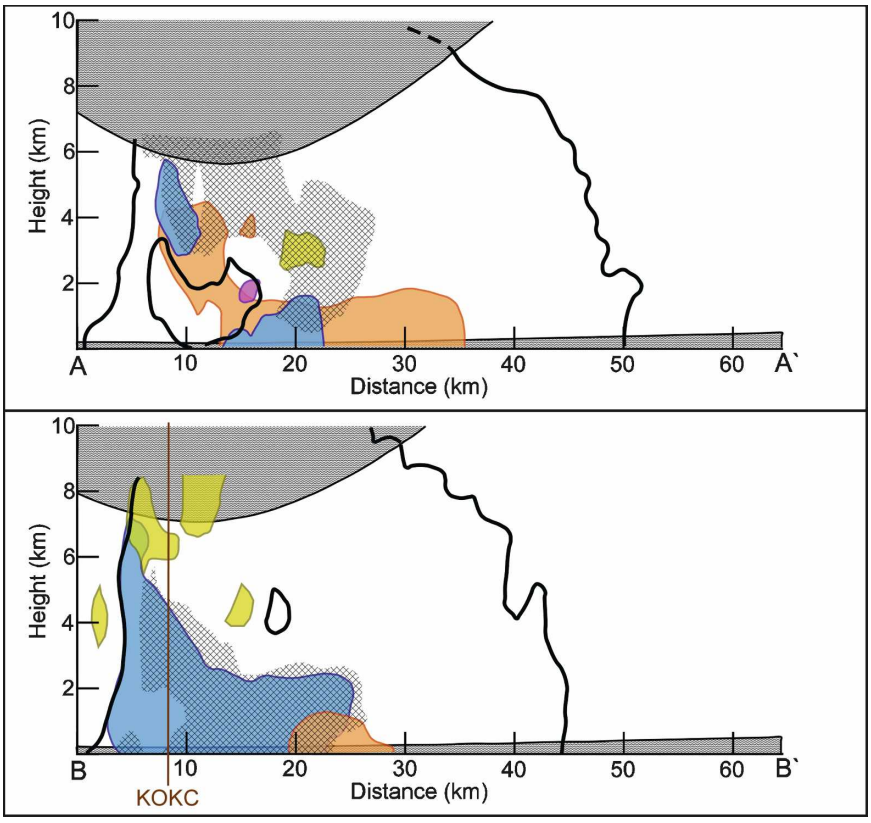


FIG. 17. As in Fig. 14 but valid at 2204 UTC.

Texas, long-track "tornado 4" storm detailed in Dowell and Bluestein (2002). Also, Wakimoto and Atkins (1996) documented another open-wave gust front case with a long-track tornado near Newcastle, Texas, on 29 May 1994. As such, a hybrid of both the Lemon and Doswell and Doswell and Burgess models was supplemented with polarimetric field features noted at low and midlevels in the polarimetric observations from the storm studied in this paper.

Prominent features derived from the polarimetric fields during the mature supercell stage are graphically summarized for low and midlevels in Fig. 19. Of particular note at low levels is the highly positive $Z_{dr}$ shield along the right-forward flank of the storm. A weakly convergent boundary is shown as a FFGF along the right flank of the $Z_{dr}$ shield. Offset left and rearward of the $Z_{dr}$ shield is the $K_{dp}$ foot, which may be accompanied by large hail reports at the surface and serves as the source region for the forward-flank downdraft. Another FFGF boundary was along the right edge of the $K_{dp}$ foot, which is also the left edge of the $Z_{dr}$ shield. Both FFGF boundaries are roughly parallel to the storm motion vector. A more baroclinic RFGF boundary extends along the entire back edge of the storm approximately perpendicular to the storm motion, similar to the inferences from streamlines in the Lemon and Doswell (1979) model, approximately trailing the upshear edge of the $K_{dp}$ foot and column. At midlevels, a $Z_{dr}$ column flanks the left edge of the mesocyclone, with the $K_{dp}$ column offset farther left and flanking the $Z_{dr}$ column, right of the midlevel anticyclone (not shown). Downshear of the $K_{dp}$ column is an elongated high-reflectivity core, overlaying the $K_{dp}$ foot below. Also, downshear of the storm updraft, a negative $Z_{dr}$ region overlaid the $Z_{dr}$ shield at lower levels.

## 5. Conclusions and future work

Polarimetric radar observations from the KOUN radar of a tornadic supercell that tracked through the greater Oklahoma City, Oklahoma, metropolitan area on 8 May 2003 were examined in fine detail to extract the gross characteristics and field morphology relative to changes in storm behavior and organization. Several aspects similar to previously documented case studies of severe convection were recognized, such as the presence of midlevel $Z_{dr}$ and $K_{dp}$ columns. However, the location of these features relative to the storm updraft

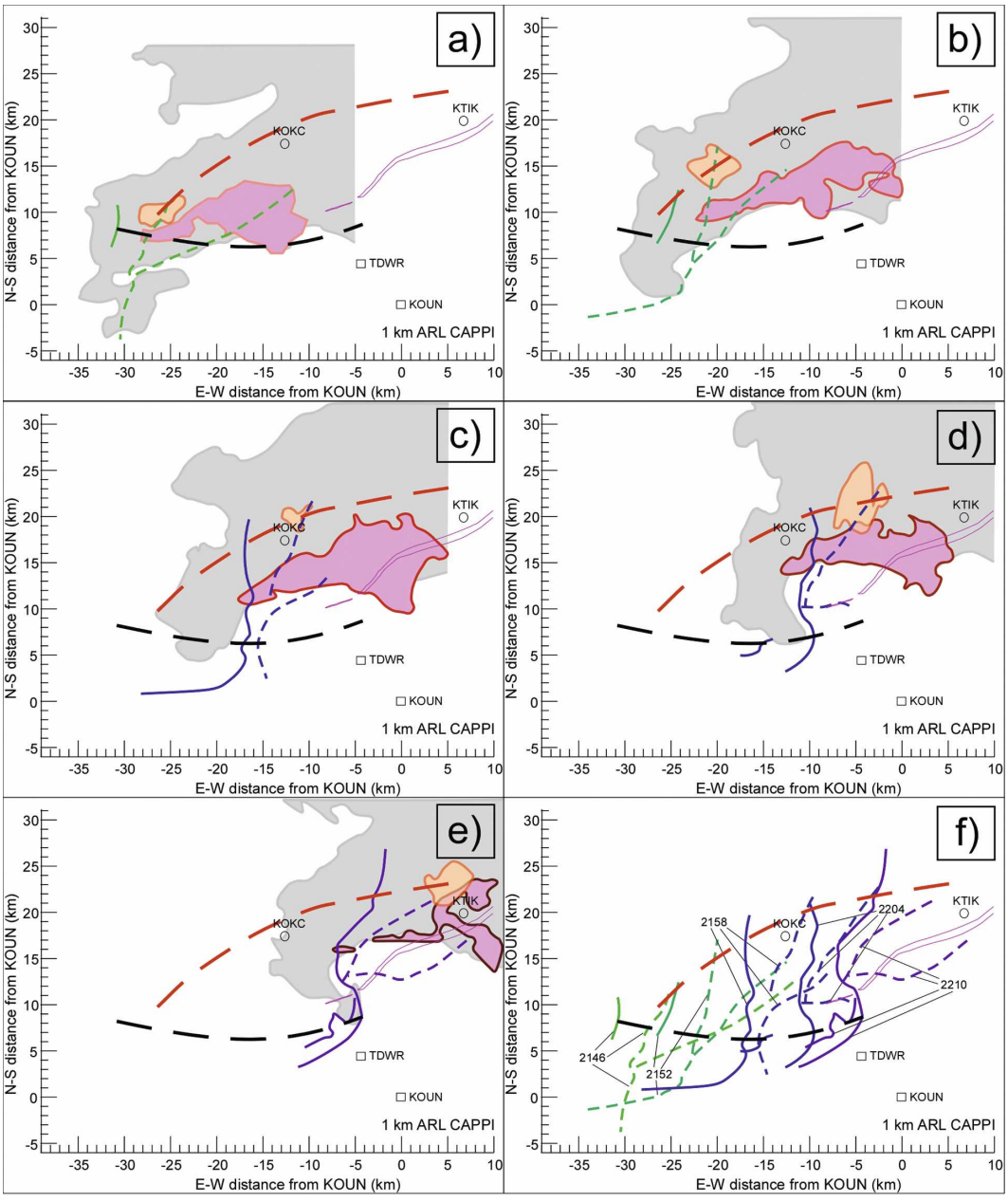


FIG. 18. (a)–(e) CAPPIs at 1 km ARL from 2146 to 2210 UTC showing evolution of ≥20 dB$Z$ echo (gray fill), $K_{dp} \geq 3^\circ$ km$^{-1}$ (orange fill), $Z_{dr} \geq 4$ dB (magenta fill), track of the $K_{dp}$ maximum centroid (heavy red dashed), track of the RFD gust front surge nose (heavy black dashed), noted convergence boundaries from multiradar radial velocity data (inferred rear-flank boundaries solid, others dashed), and tornado damage track from NWS survey (magenta contour) with (f) the latter four compounded. All plots are shown in KOUN relative coordinates in kilometers. Note the KTLX radar is located near 17.0 (10.3) in E–W (N–S) distance in kilometers (not shown).

was perhaps unique to supercells relative to previous studies of multicell storms. The transition from multicell to supercell coincided with the realignment of the $K_{dp}$ column from downshear of the $Z_{dr}$ column to the left flank. Further, the repositioning of the $K_{dp}$ column between counterrotating midlevel azimuthal shear centers aloft and midlevel convergence signatures along the left-rear flank of the storm immediately preceded the development of a rear-flank downdraft surge and subsequent tornadogenesis.

The current study has also identified a few new features from the polarimetric radar observations. First,

TABLE 3. KOUN sounding and surface observation thermodynamic values

| Height MSL (m) | Mixing ratio (g kg$^{-1}$) | Potential temperature (K) | Equivalent potential temperature (K) | Wet-bulb potential temperature (K) |
|---|---|---|---|---|
| 357 (surface) | 19.1 | 304.9 | 362.2 | 299.69 |
| 394 (F-TIK) | 20.0 | 302.0 | 361.4 | 299.56 |
| 397 (F-OKC) | 18.8 | 303.1 | 359.2 | 299.18 |
| 610 | 17.9 | 305.2 | 359.1 | 299.17 |
| 686 | 17.6 | 305.3 | 358.1 | 299.00 |
| 914 | 17.2 | 305.5 | 357.3 | 298.86 |
| 1114 | 16.9 | 305.6 | 356.5 | 298.72 |
| 1219 | 15.4 | 306.7 | 353.4 | 298.16 |
| 1426 | 12.8 | 309.1 | 348.3 | 297.24 |
| 397 (R-OKC) | 14.6 | 299.0 | 341.8 | 296.00 |
| 394 (R-TIK) | 14.6 | 297.9 | 340.4 | 295.73 |
| 1829 | 8.3 | 310.7 | 336.6 | 294.95 |
| 2134 | 5.9 | 311.8 | 330.5 | 293.68 |

the presence of a large area of highly positive $Z_{dr}$ ($Z_{dr}$ shield) at low levels was found along the right flank of the storm during the supercell phase. While another study noted the highest $Z_{dr}$ values were immediately downshear of the storm updraft (Ryzhkov et al. 2005), here we focus on the broader expanse of relatively high positive $Z_{dr}$ (where $K_{dp}$ also remains low), indicative of an expanse of sparse large drops along the right flank of the storm, where evaporation rates would be relatively small. A weakly convergent boundary was noted along the right flank of the $Z_{dr}$ shield. Next, a low-level downshear extension of high $K_{dp}$ from the $K_{dp}$ column aloft was identified as a $K_{dp}$ foot. The track of the $K_{dp}$ foot coincided with surface reports of large hail. Further, the low-level $K_{dp}$ maximum tracked with the apparent forward-flank downdraft center as indicated by low-level radial divergence, with a weak convergent boundary at low levels along the right flank of the $K_{dp}$ foot, which was also the left flank of the $Z_{dr}$ shield.

Samples from observations in the forward-flank downdraft, despite some having high liquid water content present, were found to have thermodynamic characteristics quite similar to the surface layer conditions of the environment sounding profile. This suggested that the forward-flank downdraft source height was likely entirely below the capping inversion. The rear-flank downdraft samples were only from left of the eventual tornado track, though behind a continuous gust front along the back edge of the storm, immediately trailing the $K_{dp}$ foot. These samples suggested the rear-flank air must have had significant quantities of air drawn down from above the capping inversion, where similarly cool wet-bulb potential temperature conditions were found. The rear-flank downdraft was quite cold in contrast to recent studies suggestive of warm rear-flank downdrafts as being more conducive to significantly tornadic storms.

The $K_{dp}$ maximum was observed to track along a clockwise arc from the left-rear edge of the $Z_{dr}$ maximum to the left-forward (downshear) edge of the $Z_{dr}$ maximum as the storm transitioned into the tornadic phase. Consistently, the FFGF boundaries were also

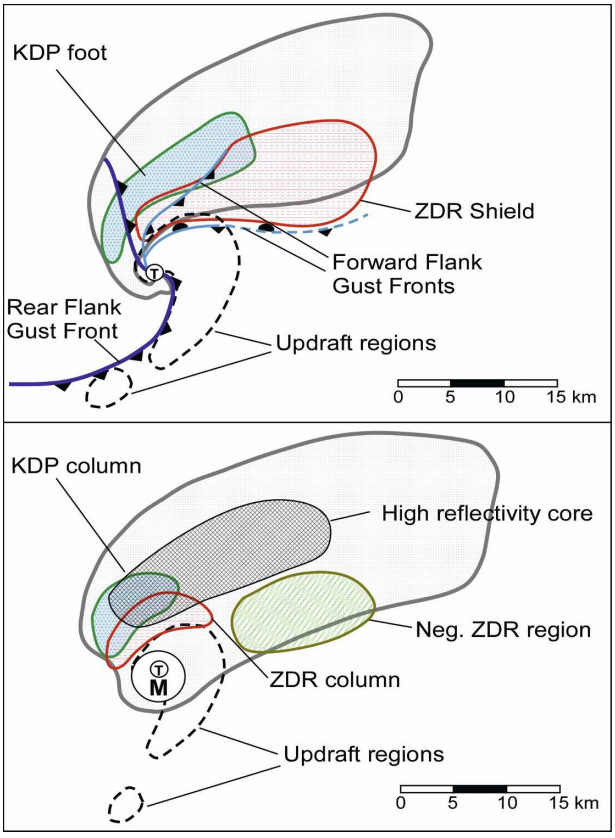


FIG. 19. Conceptual model of (top) 1 km AGL and (bottom) midlevel polarimetric radar features conceptualized for a tornadic classic supercell storm based on observations of the 8 May 2003 OKC tornadic storm. Adapted from a composite of Doswell and Burgess's (1993) Fig. 3a and Lemon and Doswell's (1979) Fig. 7.

observed to rotate in a clockwise direction during this interval. Still, the FFGFs converged and intersected the RFGF well left of RFGF surge, with the tornado cyclone developing not at the location of the merging gust fronts but just left of the gust front surge nose.

Whether the evolution shown for this event is an appropriate conceptual model for other tornadic supercells should be assessed to determine the possible utility of observing polarimetric field trends in anticipating changes in storm behavior. A recent investigation by Kumjian and Ryzhkov (2007) of polarimetric features within numerous supercell storms suggested broad storm-scale features noted in this study are common to supercell storm features in their wider, though less detailed, investigation. In particular, their study did not look at the temporal evolution of polarimetric fields, and as such the generality of the evolution described in this study and whether this evolution can serve as a precursor of storm behavior remains unknown. Future studies of polarimetric signatures associated with supercell storms, coupled with surface observations such as those from mobile mesonets, could explore whether the width of the $Z_{dr}$ shield along the right-forward flank of supercell storms was useful as a proxy to baroclinicity along the FFGF, whether the large hail swath is commonly associated with the $K_{dp}$ foot track, and if repositioning of the $K_{dp}$ column is common prior to the development of rear-flank downdraft surges. Then, polarimetric observations might provide supplemental information for assessing potential hazards and highlight regions within a storm at the greatest risk for hazardous weather conditions. Further study of polarimetric variable trends could enable our ability to detect storm hazards prior to their occurrence (e.g., Scharfenberg et al. 2003) and beyond just their identification (e.g., Ryzhkov et al. 2005).

Preliminary efforts in ensemble Kalman filter based storm-scale polarimetric radar assimilation suggest a potentially greater significance to polarimetric radar information, to be reported upon in future publications. Physical ties between storm kinematics and polarimetric field evolution, as evolved by the governing equations of the assimilation system, offer the opportunity to enhance estimates of the atmospheric state variables. Further, improved or new microphysical parameterizations in numerical models guided by polarimetric observations are expected to enable a refined understanding of the role of microphysics in downdraft forcing and in the subsequent thermodynamic character of downdraft air. In turn, this work could then reinforce polarimetric field morphology precursors to changes in storm behavior and provide a greater understanding of the internal workings of supercell storms.

*Acknowledgments.* This material is based on work supported by the National Science Foundation under Award ATM-0449753 for the first and third authors. Funding for the second author was provided by NOAA/Office of Oceanic and Atmospheric Research under NOAA–University of Oklahoma Cooperative Agreement NA17RJ1227, the U.S. Department of Commerce, and NSF Grant ATM-0437898. David Dowell graciously provided cleaned reflectivity and dealiased velocity data from the KOUN radar used in this study, as well as the objective analysis software utilized for the radar analysis. Kevin Scharfenberg provided additional KOUN data and Valery Melnikov along with Scott Giangrande supplied radar calibration information. Kevin Scharfenberg also provided helpful discussions on polarimetric radar signatures of microbursts. Kevin Manross prepared the TDWR and KTLX radar data used in this study. Steve Nesbitt provided helpful discussions on polarimetric observation quality control issues. Rit Carbone and another anonymous reviewer offered many helpful suggestions. Some plots were generated using NCAR Command Language software.

## REFERENCES

Balakrishnan, N., and D. S. Zrnić, 1990: Use of polarization to characterize precipitation and discriminate large hail. *J. Atmos. Sci.,* **47,** 1525–1540.

Brandes, E. A., J. Vivekanandan, J. D. Tuttle, and C. J. Kessinger, 1995: A study of thunderstorm microphysics with multiparameter radar and aircraft observations. *Mon. Wea. Rev.,* **123,** 3129–3143.

Bringi, V. N., and C. Chandrasekar, 2001: *Polarmetric Doppler Weather Radar.* Cambridge University Press, 636 pp.

——, J. Vivekanandan, and J. D. Tuttle, 1986: Multiparameter radar measurements in Colorado convective storms. Part II: Hail detection studies. *J. Atmos. Sci.,* **43,** 2564–2577.

Brooks, H. E., C. A. Doswell III, and R. B. Wilhelmson, 1994: The role of midtropospheric winds on the evolution and maintenance of low-level mesocyclones. *Mon. Wea. Rev.,* **122,** 126–136.

Browning, K. A., 1964: Airflow and precipitation trajectories within severe local storms which travel to the right of the winds. *J. Atmos. Sci.,* **21,** 634–639.

Burgess, D. W., 2004: High resolution analyses of the 8 May 2003 Oklahoma City storm, part 1: Storm structure and evolution from radar data. Preprints, *22nd Conf. on Severe Local Storms,* Hyannis, MA, Amer. Meteor. Soc., 12.4. [Available online at http://ams.confex.com/ams/pdfpapers/81939.pdf.]

——, and M. A. Magsig, 1993: Evolution of the Red Rock, Oklahoma supercell of April 26, 1991. Preprints, *17th Conf. on Severe Local Storms,* St. Louis, MO, Amer. Meteor. Soc., 257–261.

——, and ——, 1998: Recent observations of tornado development at near range to WSR-88D radars. Preprints, *19th Conf. on Severe Local Storms,* Minneapolis, MN, Amer. Meteor. Soc., 756–759.

Conway, J. W., and D. S. Zrnić, 1993: A study of embryo produc-

tion and hail growth using dual-Doppler and multiparameter radars. *Mon. Wea. Rev.,* **121,** 2511–2528.

Cressman, G. P., 1959: An operational objective analysis system. *Mon. Wea. Rev.,* **87,** 367–374.

Crum, T. D., and R. L. Alberty, 1993: The WSR-88D and the WSR-88D Operational Support Facility. *Bull. Amer. Meteor. Soc.,* **74,** 1669–1687.

Doswell, C. A., III, and D. W. Burgess, 1993: Tornadoes and tornadic storms: A review of conceptual models. *The Tornado: Its Structure, Dynamics, Prediction, and Hazards, Geophys. Monogr.,* Vol. 79, Amer. Geophys. Union, 161–172.

——, S. J. Weiss, and R. H. Johns, 1993: Tornado forecasting: A review. *The Tornado: Its Structure, Dynamics, Prediction, and Hazards, Geophys. Monogr.,* Vol. 79, Amer. Geophys. Union, 557–571.

Doviak, R. J., V. Bringi, A. Ryzhkov, A. Zahrai, and D. Zrnić, 2000: Considerations for polarimetric upgrades to operational WSR-88D radars. *J. Atmos. Oceanic Technol.,* **17,** 257–278.

Dowell, D. C., and H. B. Bluestein, 2002: The 8 June 1995 McLean, Texas, storm. Part II: Cyclic tornado formation, maintenance, and dissipation. *Mon. Wea. Rev.,* **130,** 2649–2670.

——, L. J. Wicker, and D. J. Stensrud, 2004: High resolution analyses of the 8 May 2003 Oklahoma City storm. Part II: EnKF data assimilation and forecast experiments. Preprints, *22nd Conf. on Severe Local Storms,* Hyannis, MA, Amer. Meteor. Soc.,. 12.5. [Available online at http://ams.confex.com/ams/pdfpapers/81393.pdf.]

Grzych, M. L., B. D. Lee, and C. A. Finley, 2007: Thermodynamic analysis of supercell rear-flank downdrafts from Project ANSWERS. *Mon. Wea. Rev.,* **135,** 240–246.

Hall, M. P. M., J. W. F. Goddard, and S. M. Curry, 1984: Identification of hydrometeors and other targets by dual-polarization radar. *Radio Sci.,* **19,** 132–140.

Hamill, T. M., R. S. Schneider, H. E. Brooks, G. S. Forbes, H. B. Bluestein, M. Steinberg, D. Meléndez, and R. M. Dole, 2005: The May 2003 extended tornado outbreak. *Bull. Amer. Meteor. Soc.,* **86,** 531–542.

Hu, Z., and R. C. Srivastava, 1995: Evolution of raindrop size distribution by coalescence, breakup, and evaporation: Theory and observations. *J. Atmos. Sci.,* **52,** 1761–1783.

Hubbert, J., V. N. Bringi, and L. D. Carey, 1998: CSU-CHILL polarimetric measurements from a severe hailstorm in eastern Colorado. *J. Appl. Meteor.,* **37,** 749–775.

Illingworth, A. J., J. W. F. Goddard, and S. M. Cherry, 1987: Polarization radar studies of precipitation development in convective storms. *Quart. J. Roy. Meteor. Soc.,* **113,** 469–489.

Jameson, A. R., 1985: Microphysical interpretation of multiparameter radar measurements in rain. Part III: Interpretation and measurement of propagation differential phase shift between orthogonal linear polarizations. *J. Atmos. Sci.,* **42,** 607–614.

Knupp, K. R., 1988: Downdrafts within high plains cumulonimbi. Part II: Dynamics and thermodynamics. *J. Atmos. Sci.,* **45,** 3965–3982.

Kumjian, M., and A. Ryzhkov, 2007: Polarimetric characteristics of tornadic and nontornadic supercell thunderstorms. Preprints, *33rd Int. Conf. on Radar Meteorology,* Cairns, QLD, Australia, Amer. Meteor. Soc., P10.1. [Available online at http://ams.confex.com/ams/pdfpapers/122882.pdf.]

Lee, B. D., B. F. Jewett, and R. B. Wilhelmson, 2006: The 19 April 1996 Illinois tornado outbreak. Part II: Cell mergers and associated tornado incidence. *Wea. Forecasting,* **21,** 449–464.

Lemon, L. R., and C. A. Doswell, 1979: Severe thunderstorm evolution and mesocyclone structure as related to tornadogenesis. *Mon. Wea. Rev.,* **107,** 1184–1197.

Loney, M. L., D. S. Zrnić, J. M. Straka, and A. V. Ryzhkov, 2002: Enhanced polarimetric radar signatures above the melting level in a supercell storm. *J. Appl. Meteor.,* **41,** 1179–1194.

Markowski, P. M., 2002: Hook echoes and rear-flank downdrafts: A review. *Mon. Wea. Rev.,* **130,** 852–876.

——, J. M. Straka, and E. N. Rasmussen, 2002: Direct surface thermodynamic observations within the rear-flank downdrafts of nontornadic and tornadic supercells. *Mon. Wea. Rev.,* **130,** 1692–1721.

Miller, R. C., 1972: Notes on the analysis and severe-storm forecasting procedures of the Air Force Global Weather Central Tech. Rep. 200 (rev.), Air Weather Service, Scott Air Force Base, IL, 190 pp.

NCDC, 2003: *Storm Data.* Vol. 45, No. 5. [Available from the National Climatic Data Center, 151 Patton Ave., Asheville, NC 28801.]

Pruppacher, H. R., and J. D. Klett, 1997: *Microphysics of Clouds and Precipitation.* 2nd ed. Kluwer Academic Publications, 954 pp.

Rosenfeld, D., and C. W. Ulbrich, 2003: Cloud microphysical properties, processes, and rainfall estimation opportunities. *Radar and Atmospheric Science: A Collection of Essays in Honor of David Atlas, Meteor. Monogr.,* No. 52, Amer. Meteor. Soc., 237–258.

Rotunno, R., and J. B. Klemp, 1982: The influence of the shear-induced pressure gradient on thunderstorm motion. *Mon. Wea. Rev.,* **110,** 136–151.

Ryzhkov, A. V., T. J. Schuur, D. W. Burgess, and D. S. Zrnić, 2005: Polarimetric tornado detection. *J. Appl. Meteor.,* **44,** 557–570.

——, and Coauthors, 2007: Comparison of polarimetric algorithms for hydrometeor classification at S and C bands. Preprints, *33rd Conf. on Radar Meteorology,* Cairns, QLD, Australia, Amer. Meteor. Soc., 10.3. [Available online at http://ams.confex.com/ams/pdfpapers/123109.pdf.]

Sachidananda, M., and D. S. Zrnić, 1987: Rain rate estimates from differential polarization measurements. *J. Atmos. Oceanic Technol.,* **4,** 588–598.

Scharfenberg, K. A., 2002: Polarimetric radar signatures in damaging downburst-producing thunderstorms. M.S. thesis, Dept. of Meteorology, University of Oklahoma, 134 pp.

——, M. P. Foster, and D. L. Andra, 2003: Operational uses of polarimetric radar data in severe local storm prediction. Preprints, *31st Int. Conf. on Radar Meteorology,* Seattle, WA, Amer. Meteor. Soc., P4B.3. [Available online at http://ams.confex.com/ams/pdfpapers/64415.pdf.]

——, and Coauthors, 2005: The Joint Polarization Experiment: Polarimetric radar in forecasting and warning decision making. *Wea. Forecasting,* **20,** 775–788.

Schuur, T. J., A. V. Ryzhkov, D. S. Zrnić, and M. Schönhuber, 2001: Drop size distributions measured by a 2D video disdrometer: Comparison with dual-polarization radar data. *J. Appl. Meteor.,* **40,** 1019–1034.

——, P. Heinselman, K. Scharfenberg, A. Ryzhkov, D. Zrnić, V. Melnikov, and J. Krause, 2003: Overview of the Joint Polarization Experiment (JPOLE). National Severe Storms Laboratory Rep., Norman, OK, 39 pp. [Available online at http://

cimms.ou.edu/~schuur/jpole/JPOLE_Overview_Report.pdf.]

Seliga, T. A., and V. N. Bringi, 1976: Potential use of radar differential reflectivity measurements at orthogonal polarizations for measuring precipitation. *J. Appl. Meteor.,* **15,** 69–76.

Shabbott, C. J., and P. M. Markowski, 2006: Surface in situ observations within the outflow of forward-flank downdrafts of supercell thunderstorms. *Mon. Wea. Rev.,* **134,** 1422–1441.

Smith, T. M., K. L. Elmore, G. J. Stumpf, and V. Lakshmanan, 2003: Detection of rotation and boundaries using two-dimensional, local, linear least squares estimates of velocity derivatives. Preprints, *31st Conf. on Radar Meteorology,* Seattle, WA, Amer. Meteor. Soc., P2C.9. [Available online at http://ams.confex.com/ams/pdfpapers/64420.pdf.]

Srivastava, R. C., 1987: A model of intense downdrafts driven by the melting and evaporation of precipitation. *J. Atmos. Sci.,* **44,** 1752–1774.

Straka, J. M., D. S. Zrnić, and A. V. Ryzhkov, 2000: Bulk hydrometeor classification and quantification using polarimetric radar data: Synthesis of relations. *J. Appl. Meteor.,* **39,** 1341–1372.

Ulbrich, C. W., and D. Atlas, 2007: Microphysics of raindrop size spectra: Tropical continental and maritime storms. *J. Appl. Meteor. Climatol.,* **46,** 1777–1791.

Vasiloff, S. V., 2001: Improving tornado warnings with the Federal Aviation Administration's terminal Doppler weather radar. *Bull. Amer. Meteor. Soc.,* **82,** 861–874.

Wakimoto, R. M., and V. N. Bringi, 1988: Dual-polarization observations of microbursts associated with intense convection: The 20 July storm during the MIST Project. *Mon. Wea. Rev.,* **116,** 1521–1539.

——, and N. T. Atkins, 1996: Observations on the origins of rotation: The Newcastle tornado during VORTEX 94. *Mon. Wea. Rev.,* **124,** 384–407.

——, and H. Cai, 2000: Analysis of a nontornadic storm during VORTEX 95. *Mon. Wea. Rev.,* **128,** 565–592.